Preparation and characterization of zinc ferrite-Polyaniline-Graphene oxide nanocomposite for removal of Orange G and Malachite green dye from aqueous solution: as a model of water treatment and health environment

Zain Al-Abidine Naji Al-Hasnawy[1], Khawla Kani Jasim[2], Masar Ali Awad[3]
[1,2,3] Department of Chemistry, College of Science, Al-Muthanna University, Iraq
Email: zeinalabdeen.naji.scih@mu.edu.iq,

Abstract
In the present study, $ZnFe_2O_4$ nanoparticles were synthesized using an ultrasound- assisted Co-precipitation method and $ZnFe_2O_4$-PANI-GO nanocomposite was synthesized by in situ oxidative polymerization to form a three-dimensional network structure. The characterization of prepared nanomaterials was done through different techniques such as X-ray diffraction (XRD), Field Emission Scanning Electron Microscope (FE-SEM), elemental analyses (EDS & elemental mapping), Vibrating-Sample Magnetometer (VSM), Surface area analysis (BET & BJH), Fourier Transform Infrared Spectroscopy (FT-IR), Atomic Force Microscope (AFM), and thermogravimetric analysis (TGA). PANI, GO, and $ZnFe_2O_4$ ternary nanomaterials are wrapped together to form a three-dimensional porous nanostructure and homogeneously dispersed according to the EDS, elemental mapping, and FE-SEM images. The FT-IR Spectroscopy exhibits the emergence and shifts in the main bands and in addition XRD which the average it's crystal sizes (19.35 nm) for $ZnFe_2O_4$-PANI-GO are different from $ZnFe_2O_4$. Moreover, $ZnFe_2O_4$-PANI-GO was studied as an adsorbent to show (OG and MG dyes) adsorption from an aqueous solution. Thermodynamic factors ($\Delta G°$, $\Delta H°$, and $\Delta S°$) concluded that the adsorption of both dyes was spontaneous in nature and exothermic. The adsorption pursued pseudo-second-order kinetics. In addition, the isotherm models Freundlich, Langmuir, and Timken were used to model the experimental adsorption data. To match the experimental isotherm, the Langmuir isotherm was utilized.

Keywords: Nanocomposite, Zinc ferrite, Polyaniline, Graphene oxide, Adsorption, Water treatment

1. Introduction

One of the most important problems facing the globe today is pollution. In recent years, pollution has increased dramatically, reaching alarming levels in terms of its effects on living things [1]. These pollutants impact the environment, water, and soil, harming humans, plants, animals, and microbes [2]. water is the greatest grant from nature because it is essential for the existence of various biotas on our planet [3]. Maintaining its quality is a global demand that is expanding by the day because it is one of the world's limited natural resources. Sadly, many crises and conflicts over limited water supplies have occurred in the new millennium. Additionally, several water pollutants are linked to numerous human activities that are emitted into water bodies at the same time, creating serious declination in pure water [4]. Clean water scarcity will affect the agricultural, domestic, commercial, and industrial sectors. As a result of an intense contradiction between limited resources and economic progress, the current and future generations will pay a high price. There are many different types of industries, such as machinery production, printing, textiles[5], electronics, chemicals, and pharmaceutical industries are embroiled in water pollution [6]. They are in charge of the seepage of various contaminants such as dyes [7]. Wastewater is discharged from different range of industries, which comprises a variety of organic pollutants that are introduced into natural water resources, where the textile sector produces(54 %) half of the present dye effluents seen in the global environment, followed by the dyeing industries (21%), paper and pulp industries (10%), tannery and paint industries (8%), and the dye manufacturing industries (7%) [8].

A variety of technologies for eliminating dyes from water and wastewater have been developed to lessen their environmental impact. Adsorption is a widely used technique all around the world. The use of low-cost adsorbents to purify water is a viable option. Adsorption also has an advantage over other techniques in that it is a sludge-free, clean method that completely removes colors even from dilute solutions [9]. Nano-scale composite adsorbents have been increasingly popular among the vast range of adsorbents due to their higher surface area to volume ratio and which improved adsorption capability. Due to their to tiny size, high adsorption capacity, and high stability, nanoscale metal oxide and metal ferrites have recently found extensive use

doi.org/10.31838/hiv23.01.79 Received: 14.09.22, Revised: 22.10.22, Accepted: 17.12.22

as adsorbents.

Metal ferrites nanoparticles (spinel ferrites) have recently undergone modifications to enhance their physicochemical characteristics and also increased adsorption performance [10]. Due to their featured multifunctional properties, ferrite nanomaterials with a spinel structure and the general formula MFe_2O_4 (M is a divalent cation) have a wide range of applications (magnetic, dielectric, gas-sensing, dielectric, adsorptive, biomedical, catalytic) to cite a few [11]. Due to spinel ferrite particles having high surface energy, magnetic dipolar interaction, and van der Waals forces, they tend to agglomerate. Therefore, spinel ferrite has been combined with different matrix materials to fabricate nanocomposites, which leads to a performance improvement unattainable by individual materials and exhibit fewer limitations which enhances the sorption performance. The combination of spinel ferrite particles such as $ZnFe_2O_4$ with materials such as inorganic oxides, carbonaceous materials, biomaterials, and polymers has led to composites with improved performance [12].

Polyaniline (PANI) is one of the conductive polymers that contain positively charged ions on its surface and that stands out because of its outstanding electrical conductivity, facile and low cost synthesis, and high chemical stability [13]. Carbon-based systems are especially appropriate for adsorption because of their large surface area and the ability to create various functional groups, including graphene (graphene oxide or modified graphene oxide). Although carbon-based systems have a high adsorption capacity, using them in powdered form limits them from being regeneration and reusable, which limits their practical application. These disadvantages can be overcome by combining them with other materials [14]. Since graphene oxide (GO) has a high surface area, it has attracted a lot of interest as nanofillers for polymer reinforcement. It serves as a support in several catalysts and nanocomposite combinations. Oxygen-containing groups including hydroxyl, carboxyl, and epoxide groups are abundant in GO. As a result, graphene oxide becomes hydrophilic, easily dispersible in water and other solvents, and can be simply modified to be polymer compatible [15][16].

2. Materials and methods

2.1. Materials

All chemical and reagents, including aniline (which was distilled before it was used), hydrochloric acid (HCl), ferrite chloride ($FeCl_3$), zinc chloride ($ZnCl_2$), ammonium hydroxide solution (NH_4OH), ammonium peroxodisulphate ($(NH_4)_2S_2O_8$), Graphite powder, Orange G (OG) dye with following information (molecular weight: 452.4 g/mol, empirical formula: $C_{16}H_{10}N_2Na_2O_7S_2$), Malachite green (MG) dye with following information (molecular weight: 364.911 g/mol, empirical formula: $C_{23}H_{25}ClN_2$) were obtained from Sigma- Aldrich.

2.2. Preparation of Zinc Ferrite($ZnFe_2O_4$) nanoparticles

$ZnFe_2O_4$ nanoparticles were synthesized by the method of Co-precipitation. Firstly $FeCl_3$ (6.49 g, 0.04 mol) solution was mixed with $ZnCl_2$ (2.726 g, 0.02 mol) solution under aggressively stirrer for 25 min at 70°C. Secondly, ammonium solution (2M) was dropped wise to the mixture under ultrasound waves (energy 350 w, 40 kHz) until reached pH (10) and formed a brown colloidal solution. the brown precipitate was separated by centrifuge, then washed several times with hot water. Finally, $ZnFe_2O_4$ precipitate was dried in the oven at 80 ˚C overnight and then calcinated at 600 ˚C for 3hrs [17].

2.3. Preparation of Graphene oxide and $ZnFe_2O_4$-PANI-GO nanocomposite

Graphene oxide (GO) was synthesized according to the modified Hummers method [18], and PANI-$ZnFe_2O_4$-GO nanocomposite was synthesized with a ratio of (9 PANI:1 $ZnFe_2O_4$) in the presence of graphene oxide as a nanofiller material to form a three-dimensional network structure by in situ oxidative polymerizations. Firstly, (0.113) g of Zinc ferrite and (1) ml of aniline monomer are added to 100 ml of distilled water under ultrasound waves (energy 350w, 40 kHz) for 30 min to obtain a homogeneous dispersion. Secondly, added was (25) ml of (0.25) M $FeCl_3$ and (25) ml of (0.02) M HCl to the previous mixture with stirring constantly in an ice bath for 10 hrs. Thirdly, GO (0.05g) dispersed by ultrasound was added in addition to (2.75) g ammonium persulfate dropwise, and the solution was rapidly stirred again for 12 hr. Finally, the sample washing with distilled water until the nominate was colorless and then was dried for 24 hr in the oven at 50 ◦ C [19].

2.4. Characterization of PANI-$ZnFe_2O_4$-GO nanocomposite

FTIR with a wavenumber range of 400-4000 cm-1 (Shimaduz, Japan, FTIR 8400s) spectra to nanomaterials were used to determine the functional groups. The UV-Visible Spectrophotometer (UV-1800 PC Shimadzu) was used to measure the spectrum in the range of (200-800 nm). The morphology of nanomaterials was studied using a field emission scanning electron microscope (Fesem Tescan Mira3, France) with a 15 kV accelerating voltage, and the roughness of the nanocomposites' surface was measured using an angstrom AFM (SPM-AA3000, USA). The crystalline phase of samples was characterized by XRD using (BrukerAXSGmbh, Germany/D2 Phase) with CuKα radiation (0.15040nm) and the XRD pattern was recorded ranging from 5 to 80° . The surface area and porosity analysis of ZF-PANI-GO nanocomposite were obtained with Quantachrome Instruments (Nova 2200e, USA) and methods the multipoint of (BET) and (BJH). Vibrating-sample magnetometer (VSM-7300, Lake Shore) was used to measure the

saturation magnetization, and under a nitrogen atmosphere, the curve of thermogravimetric analysis (TGA) was done by Perkin Elmer (TGA 4000).

2.5.Adsorption experiments

2.5.1. Batch adsorption

Batch experiments were used to conduct OG and MG adsorption tests with PANI-ZnFe2O4-GO nanocomposite to determine the adsorption parameters, such as contact time, dose of the adsorbents, temperature, and initial pH solution, by changing one parameter at a time while other parameters are kept constant. The 1000 ppm stock solutions of OG and MG were prepared first, and then the batch adsorption solutions were prepared by diluting the stock solution. The studies were conducted in a cylindrical glass with an equivalent volume of 10 ml aqueous samples, the addition of the specified amount of the adsorbent's surface to known initial concentrations of OG or MG. To study the impact of solution pH, certain amounts of distilled water with a specific pH level (modified with dilute HCl or NaOH) were added to the OG and MG solutions. On a shaker water bath, the solutions were aggressively stirred at 120 rpm for the required period of time to reach equilibrium. After the separation of the suspended material, UV-Visible spectroscopy at λ max nm for each dye was used to calculate the equilibrium concentration of the solution. At the equilibrium time, the quantity and removal percentage of dye adsorbed on the adsorbent surface were determined using equations 1 and 2, respectively.

$$q_e = \frac{V(C_0 - C_e)}{m} \quad (1)$$

$$\text{Removal}(\%) = \frac{C_0 - C_e}{C_0} \times 100 \quad (2)$$

Where Co and Ce are the initial and final concentrations (mg/L) of OG and MG dye in an aqueous solution, respectively. qe (mg g-1), is the amount of OG and MG adsorbed on fixed adsorbent mass (g) at the time of equilibrium. V is the volume (in L) of the initial OG and MG solution.

3. Results and Discussion

3.1. Characterization

Functional groups

The existence of functional groups and the nature of molecular bonds in the material can be determined using FT-IR. The FT-IR spectrum of ZF nanoparticles, GO, PANI, and ZF-PANI-GO nanocomposite can be characterized. The ZnFe2O4 spectrum in Fig. 1, shows the following peaks: The two broad peaks, the first are assigned to the vibrational bond at 551.66 cm-1 relates to the metal at the tetrahedral site (Zn-O) possessing inherent stretching vibrations, whilst the second is assigned to the vibrational bond at 435.93 cm-1 corresponds to the octahedral metal stretching vibration (Fe-O). In addition, the stretching and bending vibrations of H-O-H bonds on the surface are endorsed by other reasonable absorption peaks at 3392.90 cm-1 and a less rigorous peak at 1647 cm-1 [20]. The GO spectrum in Fig. 2 shows the presence of oxygen in several absorption peaks as follows: The predominant absorption band at 3377.47 cm-1 is attributed to the (–OH) group stretching vibrations. Besides, the absorption peak at 1716.70 cm-1 and 1573.97 cm-1 are attributed to (C=O) stretching of carboxylic and aromatic (C=C) functional groups, respectively, whereas the two absorption peaks at 1226.77 cm-1 and 1058.96 cm-1 are attributed to epoxy (C–O) and the alkoxy (C–O), respectively [21]. While the spectrum for PANI in Fig. 3 exhibits the following peaks: The vibration of the N-H stretching is represented by the band between 3217.37 cm-1 and 3205.80 cm-1 . The stretching vibration of C=C in an asymmetrical benzene ring, corresponding to the structure of quinoid (N=Q=N) and benzene (N–B–N), is assigned at 1572.04 and 1496.81 cm-1, respectively. The two peaks at 1301.99 and 1247.99 cm-1 are caused by the stretching vibration of C-N. The characteristic absorption of PANI is the conspicuous peak at 1126.47 cm-1, which is the in-plane bending vibration of C-H produced by protonation. The characteristic absorption bands of PANI can also be found at 505.37 cm-1 (assigned to the aromatic ring of bonding mode C-N-C), 605.67 cm-1, and 690.59 cm-1 (assigned to the aromatic ring of bonding mode C-C, C-H), while the peak 813.99 cm-1 (assigned to the out-of-plane bending vibration of C-H) is also present [13].

As shown in Fig. 3 of ZnFe2O4-PANI-GO nanocomposite, all spectrums of ZnFe2O4 nanoparticles, PANI, and GO are representative in the FT-IR spectrum of prepared nanocomposite; Moreover, in the ZnFe2O4-PANI-GO nanocomposite, Amin's group appears in a higher displacement in addition to being a broad peak due to the weakness of the PANI intermolecular hydrogen bonding between its molecules after composition with ZnFe2O4 nanoparticles and GO. This indicates that there is an interaction between nanomaterials by forming a hydrogen bond [22]. On the other hand, for ternary nanocomposite where there is no peak observed at 1716.70 cm-1, maybe indicate that GO reduction occurred due to aniline polymerization and that PANI was covalently grafted on the GO surface and forming the hybrid composite [23].

crystalline structure

The crystalline structure of zinc ferrite nanoparticles and prepared nanocomposite were studied using the X-ray diffraction technique. Fig. 4 describes the XRD patterns of GO, PANI, $ZnFe_2O_4$ nanoparticles, and formed nanocomposite $ZnFe_2O_4$-PANI-GO. The XRD pattern of GO has a characteristic diffraction peak at 2θ = 11.9135°. Based on Bragg's equation, indicating a d-spacing of 0.7423 nm. During severe oxidation, water molecules intercalate between the inter-galleries of the graphite sheets, resulting in the production of oxygenated functional groups such as

hydroxyl and epoxy groups [23]. The XRD pattern reveals four characteristic peaks of PANI. A broad diffraction peak at 2θ = 15.4° and 20.2° with one weak peak at 8.7° indicate the PANI molecular chain is amorphous. While the diffraction peak at 2θ = 25.98° shows that the PANI molecular chain has a degree of crystallinity, which may be caused by doping with HCl. The hardness of the benzene ring hinders the PANI molecular chain's ability to crystallize, which is why the latter peak is not very sharp [24][13]. The $ZnFe_2O_4$ nanoparticles pattern shows diffraction peaks that are well indexed to purely cubic phase according to phase matches well with the standard JCPDS card No.22-1012 [13].

The diffracted crystal planes of ZF-PANI-GO nanocomposite were matched using the XRD patterns of ZF, GO, and PANI. The vanishing of the reflection plane at 2θ = 11.9135° for GO and the merging of the ZF and PANI planes show great interfacial interaction between the planes [19]. Furthermore, showing a combination of both diffraction peaks acquired from pure PANI and ZF, ensuring the nanocomposite's formation [25].

According to Scherrer's equation (eq.1) [13], the average crystal size of nanocomposite materials was calculated and placed in a Table (1).

$$D = \frac{k\lambda}{\beta \cos\theta} \quad (3)$$

Where: k : is the shape factor which usually takes a value of about (0.94), λ is the incident x-ray wavelength (0.15040 nm for CuK) , β is full width at half maximum (FWHM), and θ is diffraction angle at maximum intensity peak.

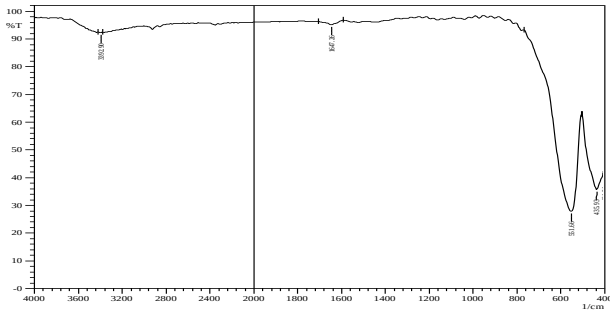

Fig. 1: FT-IR spectra of $ZnFe_2O_4$ nanoparticles

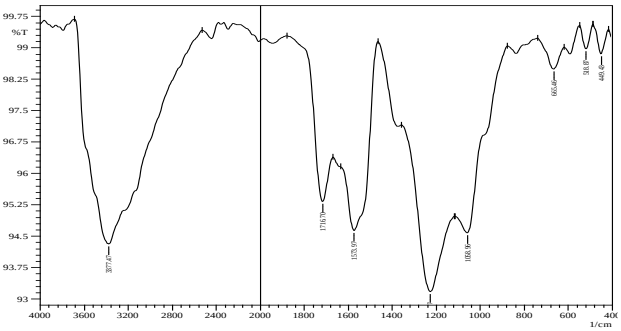

Fig. 2: FT-IR spectra of GO

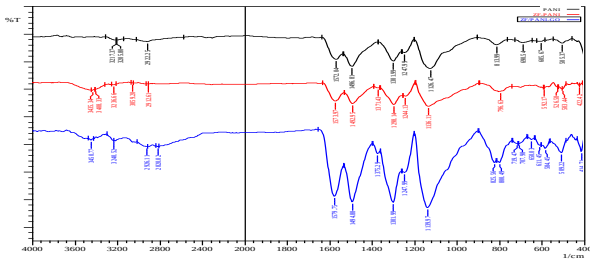

Fig. 3: FT-IR spectra of PANI, ZF-PANI, and ZF-PANI-GO nanocomposite.

Table 1: represent the average crystal sizes of $ZnFe_2O_4$ nanoparticles and prepared nanocomposite.

NO.	preparedmaterials	Peak Position (2θ)	FWHM (2θ)	average crystal sizes(nm)
1	ZnFe2O4	35.3141	0.2362	36.88
2	ZnFe2O4/PANI/GO	35.215	0.45	19.35

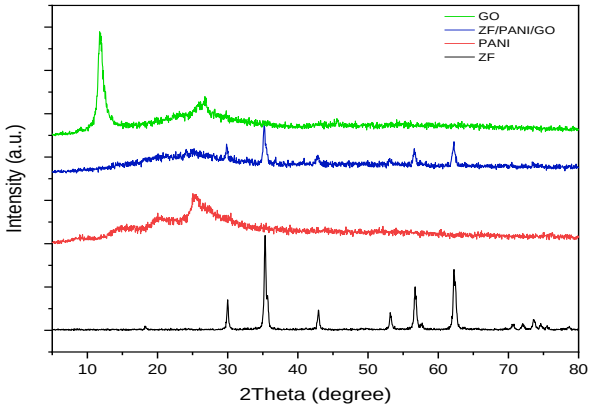

Fig.4: XRD patterns of $ZnFe_2O_4$ nanoparticles, PANI, GO, and prepared nanocomposite.

Surface topology

AFM was used to examine the surface topography of the prepared nanocomposite, PANI, and $ZnFe_2O_4$ nanoparticles. The $ZnFe_2O_4$ nanoparticles in Fig. 5(a) are characterized as having a granular shape and a fairly uniform distribution. The irregularity of the particles is caused by the agglomeration of zinc ferrite nanoparticles. While the PANI in Fig. 5(b) are irregular in shape with a heterogeneous distribution. As for the prepared nanocomposite $ZnFe_2O_4$-PANI-GO, it is less rough than PANI and this is because the $ZnFe_2O_4$ nanoparticles were wrapped with PANI which is confirmed in Fig. 4 (c) for FE-SEM images [26]. Table.2 indicates the surface roughness parameters of the prepared materials. The positive Rsk value of prepared materials assigned to the distribution of peaks is more than the valleys on the surface. Where the Rku value show two cases; spiky nature (Rku>3) shows in AFM image of zinc ferrite, and bumpy nature (Rku<3) shows in PANI and prepared nanocomposite [27][28].

Table 2: Statistical roughness parameters of zinc ferrite nanoparticles, PANI, and the $ZnFe_2O_4$-PANI-GO nanocomposite.

NO.	Prepared materials	R_a (nm)	Rsk	Rku
1	ZnFe2O4	39.876	1.917	5.677
2	PANI	134	0.666	2.527
3	ZnFe2O4/PANI/GO	64.686	0.0041	2.348

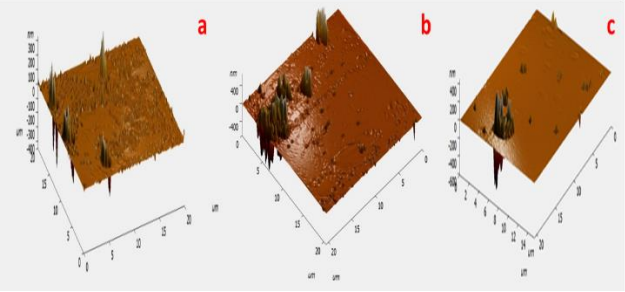

Fig. 5: The AFM images of (a) Zinc ferrite, (b) PANI, and (c) $ZnFe_2O_4$-PANI-GO nanocomposite.

Surface morphology

In the study of nanocomposites, there is a great deal of interest in the research of the size, mixing state of the components, aggregation state of the nanofiller, and morphology. As seen in Fig. 6, filed emission scanning electron microscopy was used to study the surface morphology of nanocomposites (FE-SEM). Fig. 6(a) shows the spherical shape of $ZnFe_2O_4$ nanoparticles that are randomly scattered throughout the region in the form of gatherings and are less than 100 nm in size. Furthermore, a small fraction of nanoparticles was observed to be agglomerated. Because nanomaterials have high surface energies, pore-free crystallites are present on the surface as a result of the agglomeration of small particles [17]. Additionally, Due to the usage of high temperatures (600 °C) to finish the process of Crystal growth of zinc ferrite, the calcination process also has a significant impact on the aggregation of primary particles, and it is also challenging to avoid this phenomenon. It was discovered that the zinc ferrite's typical size range was (65-75nm) [29]. While the pure PANI has a wires-like fiber network structure (nanorod) with a rough surface as shown in Fig. 6(b). Fiber chains range in length from 200 to 500 nm [10]. Fig. 6(c) shows the surface morphology of GO sheets. Structural degradation is noticed in the GO nanosheets. GO nanosheets consist of randomly aggregated in large form and long graphene oxide nanostructured sheets and stacked, and also observed Several morphologies and different microstructural [30]. The ZnFe2O4-PANI-GO nanocomposite is shown in Fig. 6(d). PANI,GO, and ZnFe2O4 ternary nanomaterials are wrapped together to form a porous nanostructure [31], which has been confirmed in Fig. (7) for EDS & elemental mapping images.

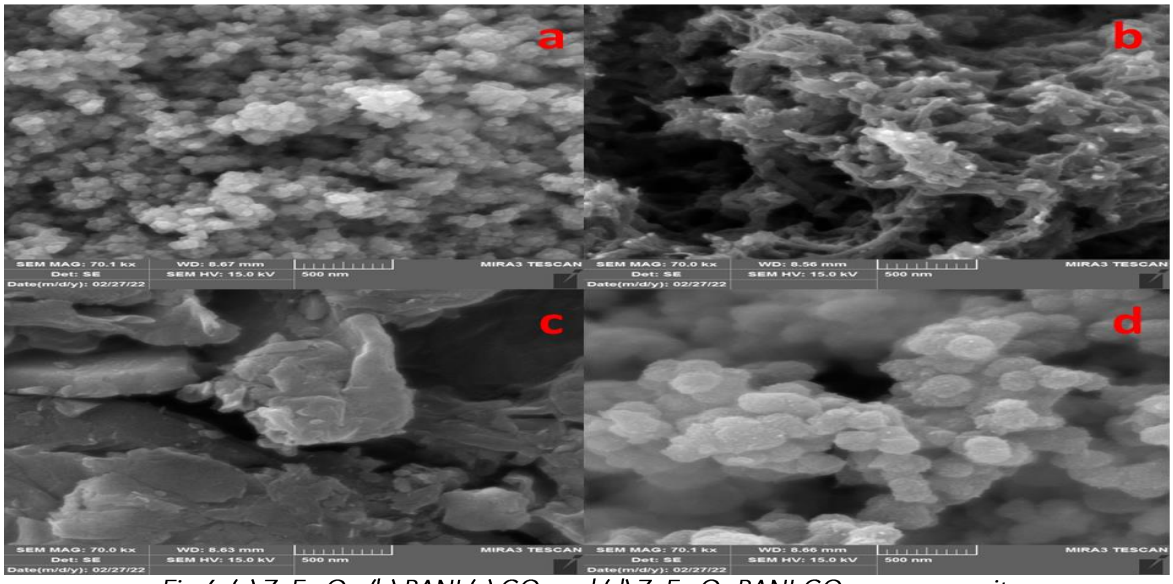

Fig.6: (a) $ZnFe_2O_4$, (b) PANI,(c) GO, and (d) $ZnFe_2O_4$-PANI-GO nanocomposite.

The elemental analyses

The elemental analyzes are shown in Fig. 7(a) by energy dispersive spectroscopy (EDS), where the $ZnFe_2O_4$-PANI-GO nanocomposite mainly consists of the elements Zn, Fe, O, C, N, S, and Cl which were confirmed by element mapping. Moreover, Fig. 7(b) shows that the above-mentioned elements were homogeneously dispersed on the surface of the nanocomposite [32][13], which indicates that the nanocomposite has been well mixed to form a three-dimensional network structure by elements mapping. The reason for the appearance of the elements sulfur and chlorine in the nanocomposite is the result of the polymerization of aniline doped with HCl and $(NH_4)_2S_2O_8$ as oxidant oxidation polymerization introduce into the nanocomposite [19].

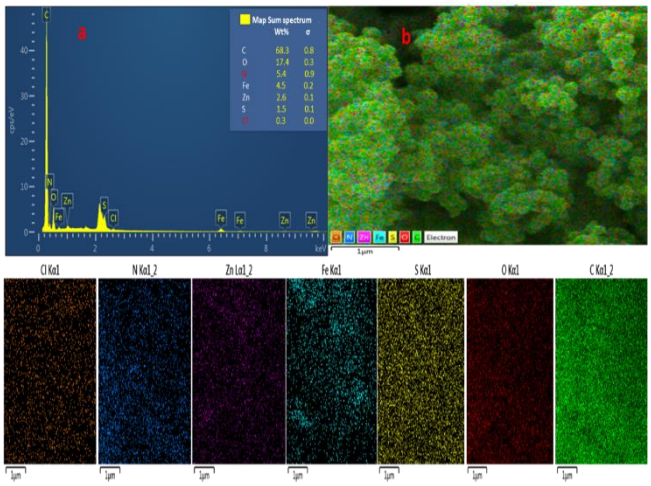

Fig. 7: EDS (a) corresponding to the FESEM and (b) element mapping of Zn, Fe, O, C, N, S, and Cl for $ZnFe_2O_4$-PANI-GO nanocomposite.

Surface area and porosity

The nitrogen adsorption-desorption isotherms of synthetic nanocomposite determined by the BET with the Pore size distribution established by the BJH are shown in Fig. 8. According to the International Union of Pure and Applied Chemistry's (IUPAC) suggested classification, the isotherms can be categorized as type IV , which denotes monolayer adsorption followed by multilayer formation and capillary condensation to mesoporous nanocomposite [33].

According to the pore configuration, the hysteresis loops can be characterized as type H3 hysteresis loops, which indicate narrow slit-shaped pores that are typically linked to sheet-like particles with non-rigid aggregates [34]. This outcome is consistent with their morphology (Fig. 6). The results of the surface area analysis (BET) are presented in Table 3, where the dispersed, nonporous, or total pore volume of pores less than 98.7808 nm and the diameter of mesoporous materials were both greater than 2 nm. Based on the average pore diameter, the results indicate that nanocomposite can be classed as mesoporous (10.25853 nm) [10].

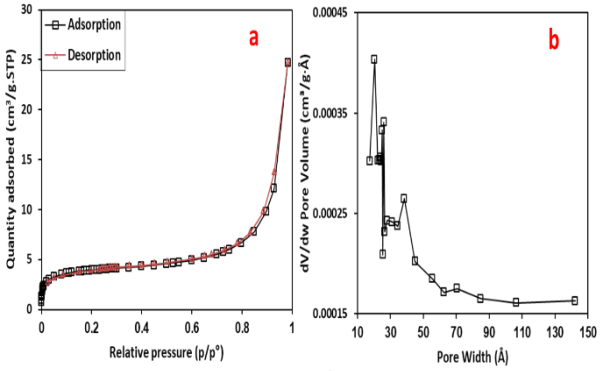

Fig. 8: (a) BET isotherms of Nitrogen adsorption-desorption of $ZnFe_2O_4$-PANI-GO nanocomposite and (b) BJH pore size distribution curve.

Table 3: Surface area, pore volume, average diameter, isotherm type, and hysteresis loop of $ZnFe_2O_4$-PANI-GO nanocomposite.

preparedmaterials	Isotherm type	Hysteresis loop	Surface area(m^2/g^{-1})	Total poreVolume ($cm^3\ g^{-1}$)	average pore diameter(nm)
ZnFe2O4/PANI/GO	4	H3	14.4579	0.037079	10.25853

Magnetic Analysis

The commonly used vibrating sample magnetometer (VSM) is a technique for determining whether an adsorbent is of magnetic nature. The saturation magnetization of $ZnFe_2O_4$-PANI-GO nanocomposite is 0.176 emu g^{-1} in a magnetic field of 1000 gauss, as shown in Fig. 9, which is less than pure $ZnFe_2O_4$ nanoparticles in previous literature [20]. The sample's magnetization curve resultantly displays hysteresis with weak ferromagnetic behavior. Additionally, spinel ferrite ($ZnFe_2O_4$) makes up a small percentage of PANI, which is clearly visible in Fig. 10 for TGA images. Therefore, the saturation magnetization value of the $ZnFe_2O_4$-PANI-GO nanocomposite will be decreased [32].

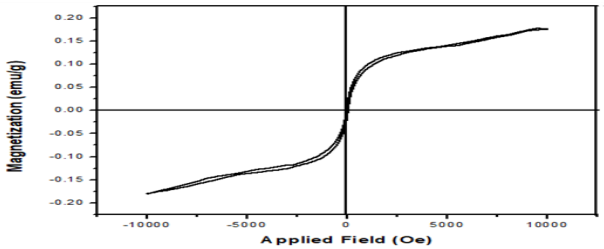

Fig. 9: VSM analysis of $ZnFe_2O_4$-PANI-GO nanocomposite.

Thermal Analysis

Fig. 10 shows the results of the Thermogravimetric analysis of the ZnFe2O4 nanoparticles and ZnFe2O4-PANI-GO nanocomposite. At temperatures between 40 and 800 °C the ZnFe2O4 nanoparticles' TGA curve exhibits one step of weight loss resulting from moisture expulsion (physically adsorbed water), which is indicative of the synthesis of pure ZnFe2O4 nanoparticles [35]. While the TGA curve of the ZF-PANI-GO nanocomposite, the thermal degradation behavior reveals two steps from weight loss; The first step indicates moisture expulsion in the temperature range of 40 to 150 °C. The second step from weight loss in the temperature range of 220-590 °C, may be a result of wrapping the nanomaterials together causing a reduction in the hydrogen bonds between the polymer chains (shifting of –NH groups that are evident in FT-IR) that leads to the degradation of the polymeric chain and its decomposition at first, followed by the decomposition of GO [13][36].

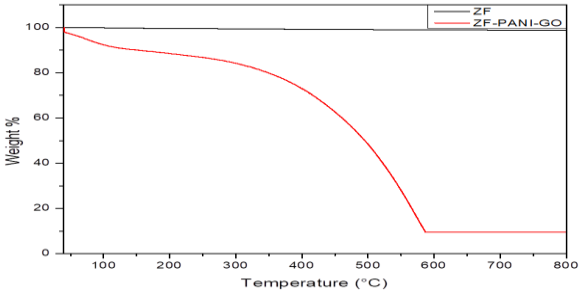

Fig. 10: TGA curves of ZnFe2O4 nanoparticles and prepared nanocomposite.

3.2. Effect of Contact Time and Adsorption Kinetics

The optimal equilibrium time to remove a specific concentration of the adsorbed dyes MG and OG by a nanocomposite surface was studied at a temperature of 25°C, a pH of 7, a constant weight of the composite of 0.01g, and at concentrations of 50 ppm and 30 ppm of both dyes OG and MG, respectively, for different time periods ranging from (5-120min). And through Fig. 11(a), the results demonstrated that the time needed to reach the equilibrium state for the OG and MG dyes was 80 min, as the amount of adsorbed dyes dramatically

increases and quickly during the first minutes of the adsorption process, after that increase will be gradual until the time needed for equilibrium, the presence of a significant number of active centers at the start of the adsorption process that is vacant and enough for the adsorption of dyes is the cause of the fast increase in the amount of adsorbed dyes. Following that, all surface active centers were occupied by dye molecule, which made the adsorption process slower and more challenging [37]. The study of adsorption kinetics is significant for pinpointing the time period of the adsorption process as well as the extent to which it affects how efficient adsorption is, and whether the adsorption rate rises or falls over time. Kinetic models were used to analyze the experimental data to investigate how the adsorbent nanocomposite's surface affects the rate of adsorption. The pseudo-first-order model and the pseudo-second-order model are the two model that describe the adsorption process the most frequently. Following are the two models are expressed in the following equations:

Model of pseudo-first-order (linear from):

$$\ln(q_e - q_t) = \ln q_e - k_1 t \quad (4)$$

Model of pseudo-second-order (linear form):

$$\frac{t}{q_t} = \frac{1}{k_2 q_e^2} + \frac{1}{q_e} t \quad (5)$$

Where qe and qt are the amounts of OG and MG adsorbed at equilibrium (mg/g) and at (t) time, k1 is the overall rate constant of pseudo-first-order kinetics (mg /(min. g)), and k2 is the pseudo-second-order rate constant (mg/ (g .min)).

As shown in Fig. 11(b) and (c) of the pseudo-first-order and pseudo-second-order models, the results explain that the adsorption process of OG and MG dyes on the nanocomposite surface follows the pseudo-second-order model through the correlation coefficients and kinetic constants calculated for both models in Table 4 [37][38].

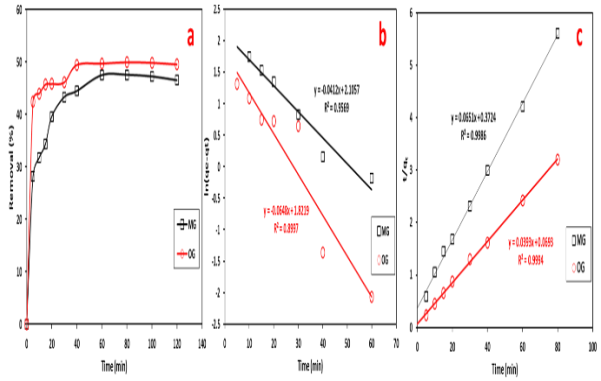

Fig. 11: The removal(%) and kinetics graphs models: (a) the removal (%) (b) pseudo-first-order and pseudo-second-order models of (c).

Table 4: The kinetic data of the OG and MG adsorption on the nanocomposite.

		First order			Second order		
Dye	$q_{e exp}$ (mg/g)	k_1 (min^{-1} mg g^{-1})	$q_{e\ cal}$ (mg/g)	R^2	k_2 (min. g/mg)	$q_{e\ cal}$ (mg/g)	R^2
OG	24.9415	0.0648	6.1836	0.8997	0.0223	25.4453	0.9994
MG	14.163	0.0412	8.2128	0.9569	0.0114	15.361	0.9986

3.3. Adsorbent dosage

Various weight were taken from the nanocomposite ranging from (0.005-0.05g), and 10 ml of dye solution at a concentration of 50 ppm of OG and 30 ppm of MG dye were added to the prepared weight at room temperature. It was observed that the adsorption process increases with the increase in the weight of the adsorbent material and that the reason for this is due to the increase in the active groups through which adsorption occurs. Though the adsorption process necessitates a balance between the adsorbent and adsorbate for all of the active centers of the adsorbate to be occupied and this, in turn, makes the adsorption process stable on the surface, the amount of adsorbent will reach its highest value after that, the significant increase in the weight of the adsorbent surface results in an unstable spread of the amount of the adsorbate molecules compared to the adsorbent surface, and this causes the adsorbed material's dissolution energy to overcome the surface's adsorption energy, which in turn causes reduced of the adsorbate molecules on the surface of the adsorbent [38][39]. The dosages utilized for all following trials were those that achieved the maximum removal of the MG dye (0.05g) and the best removal of the OG dye (0.03g). Fig. 12. Explains the impact of various weights on the adsorption process.

3.4. Adsorption isotherm studies

By stabilizing the conditions from a temperature of 25°C, a pH of 7, and concentrations of 50 ppm and 30 ppm of both OG and MG dye, respectively, an isotherm study was carried out to determine the adsorption of the dyes on the surface of the nanocomposite.

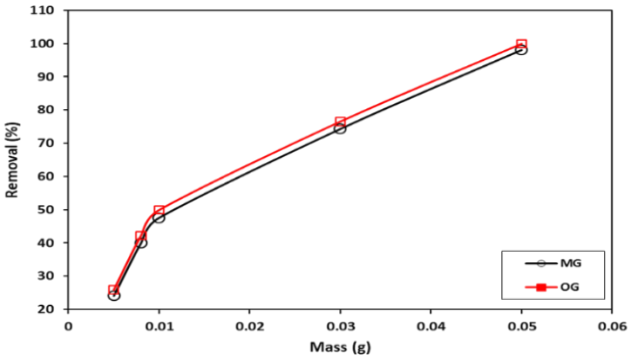

Fig. 12: Impact of various weight on the adsorption process.

Fig. 13 shows the analysis of the results of the adsorption process according to the theoretical basis of Giles's classification of adsorption isotherms. The analysis of the results reveals that the adsorption of OG and MG dye corresponds to the L4 class, or so-called Langmuir type 4 adsorption, in which the adsorption is single-layer and the orientation of the

adsorbed molecules is horizontal on the adsorbent surface [40]. The most common adsorption properties of the adsorbent are described by the Freundlich, Langmuir, and Timken isothermal equation models as follows [41]:

Model of Freundlich isotherm:

$$\log q_e = \log K_f + {}^{1}/_{n} (\log C_e) \quad (6)$$

Model of Langmuir isotherm:

$$\frac{C_e}{q_e} = \frac{C_e}{q_m} + \frac{1}{K_L q_m} \quad (7)$$

Model of Timken isotherm:

$$q_e = B_1 \ln K_T + B_1 \ln C_e \quad (8)$$

Where q_e = the amount of OG and MG adsorbed (mg/g) at C_e (equilibrium state), K_f and 1/n are Freundlich isotherm constant and intensity of adsorption, respectively. q_m and K_L are Langmuir constants related to the maximum efficiency of adsorption and energy of adsorption, respectively. B_1=RT/b, Where (T) is the temperature (at K) and (R) is the ideal gas constant (J/(mol. K)) while (b) indicates the Timken constant.

According to Table (5) and Fig. 14, the Langmuir isotherm exhibits a better fit for the adsorption of OG and MG dyes than the two models proposed by Freundlich and Timken, as noted by the correlation coefficient (R^2) values of 0.9925 and 0.9973, respectively. The compatibility of the Langmuir isotherm with the adsorption process data suggests that the adsorbing surface is homogeneous and that the active centers are of equivalent energy, and a single molecular layer of the adsorbed dye is then generated on the surface of the nanocomposite [42].

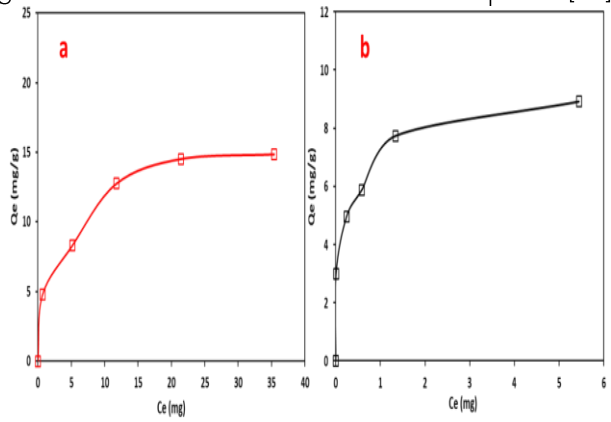

Fig. 13. Adsorption isotherm (a) OG dye (b) MG dye.

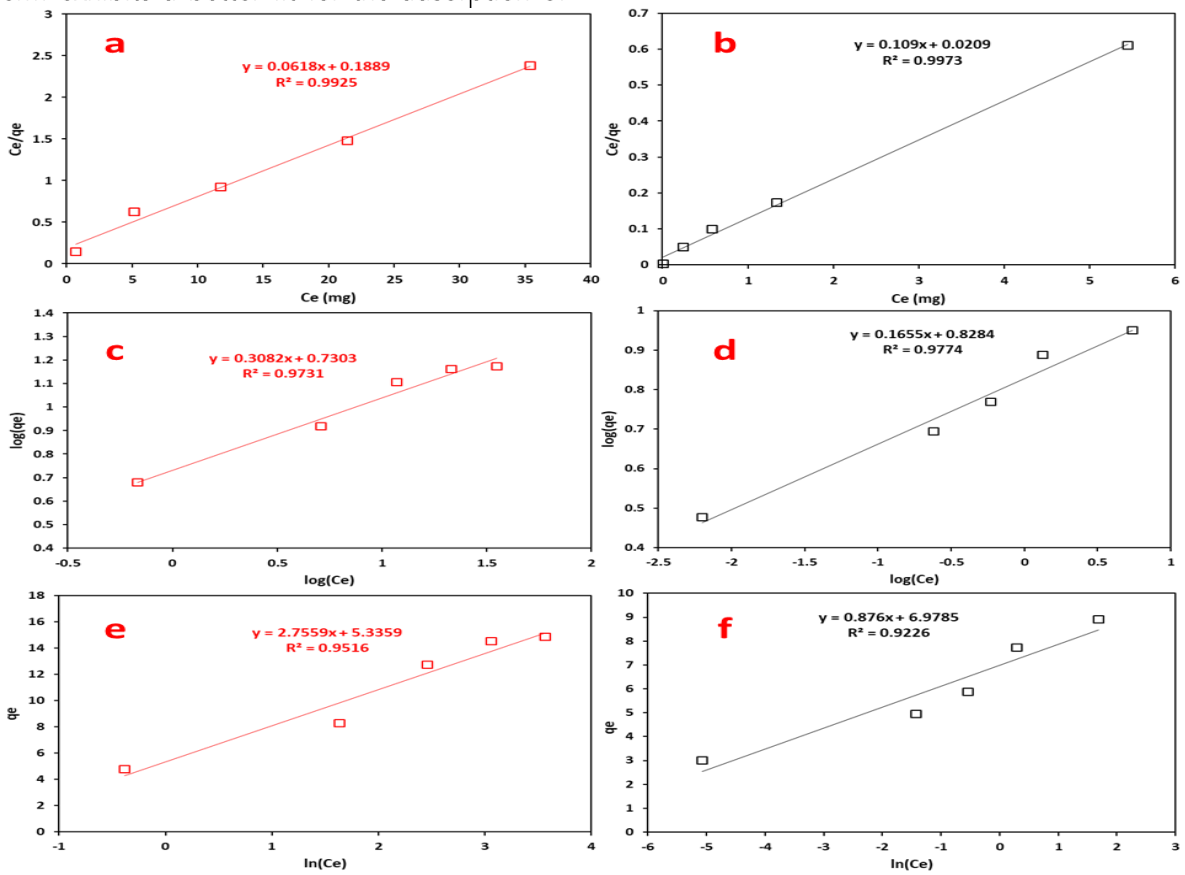

Fig. 14. Plot for adsorption (a, b) Langmuir model, (c, d) Freundlich model, and (e, f) Timken model of OG and MG dyes, respectively.

Table 5: Includes data for isotherm models of OG and MG adsorption.

	Langmuir isotherm			Freundlich isotherm			Temkin isotherm		
	Ka (L.mg-1)	qm (mg/g)	R2	KF (mg/g (L/mg)1/n)	n	R2	KT (L.g-1)	B	R2
OG	0.3272	16.1812	0.9925	5.374	3.2446	0.9731	6.9322	2.7559	0.9516
MG	5.2153	9.1743	0.9973	6.736	6.0423	0.9774	2882.243	0.876	0.9226

3.5. Initial pH effect

As shown in Fig. 15, with the stability of conditions like temperature, each dye's concentration, equilibrium time and the weight of the adsorbent surface for each dye, the effect of pH on the adsorption process of OG and MG dues were

studied on the surface of the adsorbent nanocomposite ZF-PANI-GO at specific pH values within the ranges (2,6,11).

In order to comprehend the adsorption phenomena, it is imperative to take note of the variables that influence the solution-adsorbent interface. Because it significantly affects both the surface properties of the adsorbent and the ionization state of the adsorbate molecules in solution, the solution pH is well-known as a significant parameter in the adsorption phenomenon [43]. The point of zero charge (PZC) of PANI has a substantial impact on the nanocomposite (pH PZC=7.5) of PANI. And because the proportion of the PANI matrix in the nanocomposite is high, therefore the ZF-PANI-GO surface's charge will be positively charged when the pH is below ZPC and negatively charged when the pH is above ZPC [44]. Because the OG dye molecule has pKa value of 1 and 11.5 for the deprotonation/ionization of the sulfate and hydroxyl groups, respectively, the adsorption of OG dye increases at pH = 2 and then progressively drops until it reaches pH = 10. Since the surface charge is positive of the adsorbent as a result of protonation in an acidic medium and the OG dye is a strongly negatively charged dye at an acidity greater than 1, an electrostatic attraction takes place between them. On the contrary, as the concentration of H+ ions decreases, the force of attraction also reduced (at increasing pH) At pH = 10, deprotonation of the polymer chain's nitrogen atoms and competitive interactions between the alkaline solution's OH- ions and the OG dye molecule's anions could reduce the dye's ability to bind to surfaces [45]. While the absorption of MG dye gradually rises as pH increases from 2.0 to 10.0, the cause is attributed to the gradual reduction of protonation on the adsorbed surface and the appearance of the electron pair on the nitrogen atom, which results in the occurrence of electrostatic attraction with the positive dye [41]. However, the adsorption appeared effective at all pH ranges, suggesting that electrostatic interactions were not the sole kind of interactions involved in the adsorption process. Van der Waal forces, hydrogen bonds, and the interaction between hydrophobic molecules all exist prevalent [46].

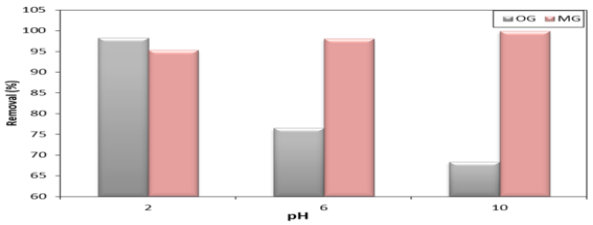

Fig. 15: The effect of pH on the adsorption of OG and MG dyes.

3.6. Thermodynamics

In this study, the parameters of thermodynamic functions were obtained to describe how OG and MG dyes adsorb on the produced composite's surface. By measuring the change in entropy (ΔS°), change in energy (ΔG°), and change in enthalpy (ΔH°) it is possible to determine the forces controlling the adsorption process, whether they be chemical or physical, as well as the direction of the reaction. Thermodynamic functions are crucial for understanding the adsorption process because they provide a good description of the nature of the regularity of the dye molecules resulting from molecular interactions. From the following equations, ΔG° , ΔH° , and ΔS° can be calculated [47]:

$$\Delta G^\circ = -RT \ln K \quad (9)$$

$$\Delta G^\circ = \Delta H^\circ - T\Delta S^\circ \quad (10)$$

From equations (9) and (10), to get equation (11)

$$\ln K = \frac{\Delta S^\circ}{R} - \frac{\Delta H^\circ}{RT} \quad (11)$$

The values of (ΔS°/R) and (-ΔH°/R) were calculated using the intercept and slope of the linear plots. MG dye and OG dye are shown in Fig. 16. The values of the thermodynamic functions for the adsorption of OG and MG dyes are shown in Table (6), and the spontaneous nature of the adsorption process was indicated by the negative value of free energy (ΔG°). The OG and MG dye adsorption process is exothermic, as shown by the negative value of enthalpy (ΔH°), which means that the mutual interaction between the dye molecules and the adsorbent surface will diminish. Furthermore, the bonds which been formed between the active centers of the adsorbent surface and the dye molecules are separated and shattered with the temperature rise [48].

Table 6: The thermodynamic parameters of adsorption of OG and MG dyes on the surface of the prepared nanocomposite.

Dye	ΔH°(KJ.mol-1)	ΔG° (J.mol-1)	ΔS° (J.mol-1.K-1)
OG	-9965.2	-2924.1	-23.47
MG	-31360.4	-9701.09	-74.02

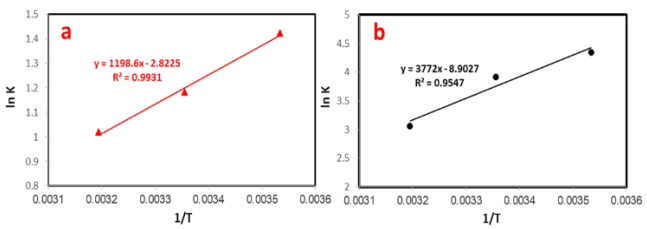

Fig. 16: Van't Hoff plots for the adsorption of (a) OG dye and (b) MG dye onto the surface of the prepared nanocomposite.

4. 4. Conclusion

In this research, ZnFe2O4 nanoparticles were synthesized using an ultrasound- assisted Co-precipitation method and ZnFe2O4-PANI-GO nanocomposite was synthesized by in situ oxidative polymerization to form a three-dimensional network structure. XRD, EDS & elemental mapping, FE-SEM, BET & BJH, FT-IR, AFM, and TGA ware used to

characterize the nanocomposite of (ZnFe2O4-PANI-GO). The resultant nanocomposite was used to remove Orange G dye and Malachite green dye from an aqueous solution. The removal efficiency of OG and MG reached a maximum at pH 2 and 10, respectively, while the adsorption rate rose significantly when the dosage of adsorbent was increased to both two dyes. The results indicated for both the two dyes that the adsorption process followed a pseudo-second-order model and that provided a better explanation of the kinetic adsorption. The adsorption behavior and the equilibrium data were represented by the Langmuir isotherm model. The ZnFe2O4-PANI-GO nanocomposite used for OG and MG adsorption was exothermic and spontaneous, according to the thermodynamic study.

References

[1] M. Naz et al., "Elimination of dyes by catalytic reduction in the absence of light: A review," J. Mater. Sci., vol. 56, no. 28, pp. 15572–15608, 2021, doi: 10.1007/s10853-021-06279-1.

[2] T. K. F. S. Freitas, C. A. Almeida, D. D. Manholer, H. C. L. Geraldino, M. T. F. de Souza, and J. C. Garcia, Review of Utilization Plant-Based Coagulants as Alternatives to Textile Wastewater Treatment. 2018. doi: 10.1007/978-981-10-4780-0_2.

[3] N. Mikosch, "Spatial Resolution in Water Footprinting : from Global to Local Scale," no. August, 2021.

[4] A. M. Elgarahy, K. Z. Elwakeel, S. H. Mohammad, and G. A. Elshoubaky, "A critical review of biosorption of dyes, heavy metals and metalloids from wastewater as an efficient and green process," Clean. Eng. Technol., vol. 4, no. June, p. 100209, 2021, doi: 10.1016/j.clet.2021.100209.

[5] T. Yao, L. Qiao, and K. Du, "High tough and highly porous graphene/carbon nanotubes hybrid beads enhanced by carbonized polyacrylonitrile for efficient dyes adsorption," Microporous Mesoporous Mater., vol. 292, no. 24, p. 109716, 2020, doi: 10.1016/j.micromeso.2019.109716.

[6] S. Özdemir, S. A. Mohamedsaid, E. Kılınç, and M. Soylak, "Magnetic solid phase extractions of Co(II) and Hg(II) by using magnetized C. micaceus from water and food samples," Food Chem., vol. 271, no. Ii, pp. 232–238, 2019, doi: 10.1016/j.foodchem.2018.07.067.

[7] D. Tonato et al., "Residual biomass of Nigrospora sp. from process of the microbial oil extraction for the biosorption of procion red H–E7B dye," J. Water Process Eng., vol. 31, no. March, p. 100818, 2019, doi: 10.1016/j.jwpe.2019.100818.

[8] S. Velusamy, A. Roy, S. Sundaram, and T. Kumar Mallick, "A Review on Heavy Metal Ions and Containing Dyes Removal Through Graphene Oxide-Based Adsorption Strategies for Textile Wastewater Treatment," Chem. Rec., vol. 21, no. 7, pp. 1570–1610, 2021, doi: 10.1002/tcr.202000153.

[9] M. R. Patil and V. S. Shrivastava, "Adsorption of malachite green by polyaniline–nickel ferrite magnetic nanocomposite: an isotherm and kinetic study," Appl. Nanosci., vol. 5, no. 7, pp. 809–816, 2015, doi: 10.1007/s13204-014-0383-5.

[10] P. Das, S. Nisa, A. Debnath, and B. Saha, "Enhanced adsorptive removal of toxic anionic dye by novel magnetic polymeric nanocomposite: optimization of process parameters," J. Dispers. Sci. Technol., vol. 0, no. 0, pp. 1–16, 2020, doi: 10.1080/01932691.2020.1845958.

[11] T. Tatarchuk et al., "Synthesis, morphology, crystallite size and adsorption properties of nanostructured Mg–Zn ferrites with enhanced porous structure," J. Alloys Compd., vol. 819, no. xxxx, 2020, doi: 10.1016/j.jallcom.2019.152945.

[12] D. H. K. Reddy and Y. Yun, "Ac ce p te d t," Coord. Chem. Rev., 2016, doi: 10.1016/j.ccr.2016.01.012.

[13] J. Feng et al., "In-depth study on adsorption and photocatalytic performance of novel reduced graphene oxide-ZnFe2O4-polyaniline composites," J. Alloys Compd., vol. 681, pp. 157–166, 2016, doi: 10.1016/j.jallcom.2016.04.146.

[14] H. Hosseini, A. Zirakjou, D. J. McClements, V. Goodarzi, and W. H. Chen, "Removal of methylene blue from wastewater using ternary nanocomposite aerogel systems: Carboxymethyl cellulose grafted by polyacrylic acid and decorated with graphene oxide," J. Hazard. Mater., vol. 421, no. July 2021, p. 126752, 2022, doi: 10.1016/j.jhazmat.2021.126752.

[15] J. Fan, Z. Shi, M. Lian, H. Li, and J. Yin, "Mechanically strong graphene oxide/sodium alginate/polyacrylamide nanocomposite hydrogel with improved dye adsorption capacity," J. Mater. Chem. A, vol. 1, no. 25, pp. 7433–7443, 2013, doi: 10.1039/c3ta10639j.

[16] M. Bagheri, S. M. Jafari, and M. H. Eikani, "Ultrasonic-assisted production of zero-valent iron-decorated graphene oxide/activated carbon nanocomposites: Chemical transformation and structural evolution," Mater. Sci. Eng. C, vol. 118, no. May 2020, p. 111362, 2021, doi: 10.1016/j.msec.2020.111362.

[17] W. A. Khoso, N. Haleem, M. A. Baig, and Y. Jamal, "Synthesis, characterization and heavy metal removal efficiency of nickel ferrite nanoparticles (NFN's)," Sci. Rep., vol. 11, no. 1, pp. 1–10, 2021, doi: 10.1038/s41598-021-83363-1.

[18] N. I. Zaaba, K. L. Foo, U. Hashim, S. J. Tan, W. W. Liu, and C. H. Voon, "Synthesis of Graphene Oxide using Modified Hummers Method: Solvent Influence," Procedia Eng., vol. 184, pp. 469–477, 2017, doi: 10.1016/j.proeng.2017.04.118.

[19] Zhao J, Lin J, Xiao J, Fan H. Synthesis and electromagnetic, microwave absorbing properties of polyaniline/graphene oxide/Fe 3 O 4 nanocomposites. RSC advances. 2015;5(25):19345-52.

[20] P. A. Vinosha, L. A. Mely, J. E. Jeronsia, S. Krishnan, and S. J. Das, "Synthesis and properties of spinel ZnFe2O4 nanoparticles by facile co-

precipitation route," Optik (Stuttg)., vol. 134, pp. 99–108, 2017, doi: 10.1016/j.ijleo.2017.01.018.
[21] Y. J. Yun and K. B. Song, "Preparation and characterization of graphene oxide encapsulated gold nanoparticles," J. Nanosci. Nanotechnol., vol. 13, no. 11, pp. 7376–7380, 2013, doi: 10.1166/jnn.2013.7850.
[22] A. Mostafaei and A. Zolriasatein, "Synthesis and characterization of conducting polyaniline nanocomposites containing ZnO nanorods," Prog. Nat. Sci. Mater. Int., vol. 22, no. 4, pp. 273–280, 2012, doi: 10.1016/j.pnsc.2012.07.002.
[23] M. Achparaki et al., "We are IntechOpen , the world ' s leading publisher of Open Access books Built by scientists , for scientists TOP 1 %," Intech, p. 13, 2012, [Online]. Available: http://dx.doi.org/10.1039/C7RA00172J%0Ahttps://www.intechopen.com/books/advanced-biometric-technologies/liveness-detection-in-biometrics%0Ahttp://dx.doi.org/10.1016/j.colsurfa.2011.12.014
[24] S. A. Chen and H. T. Lee, "Polyaniline Plasticized with 1-Methyl-2-pyrrolidone: Structure and Doping Behavior," Macromolecules, vol. 26, no. 13, pp. 3254–3261, 1993, doi: 10.1021/ma00065a002.
[25] G. Singh and S. Chandra, "Nano-flowered manganese doped ferrite@PANI composite as energy storage electrode material for supercapacitors," J. Electroanal. Chem., vol. 874, p. 114491, 2020, doi: 10.1016/j.jelechem.2020.114491.
[26] M. M. Ismail, S. N. Rafeeq, J. M. A. Sulaiman, and A. Mandal, "Electromagnetic interference shielding and microwave absorption properties of cobalt ferrite CoFe2O4/polyaniline composite," Appl. Phys. A Mater. Sci. Process., vol. 124, no. 5, pp. 0–12, 2018, doi: 10.1007/s00339-018-1808-x.
[27] A. Sharifi-Viand, M. G. Mahjani, and M. Jafarian, "Determination of fractal rough surface of polypyrrole film: AFM and electrochemical analysis," Synth. Met., vol. 191, pp. 104–112, 2014, doi: 10.1016/j.synthmet.2014.02.021.
[28] N. Tayebi and A. A. Polycarpou, "Modeling the effect of skewness and kurtosis on the static friction coefficient of rough surfaces," Tribol. Int., vol. 37, no. 6, pp. 491–505, 2004, doi: 10.1016/j.triboint.2003.11.010.
[29] H. R. Saud and S. S. Al-Taweel, "New route for synthesis of pure anatase TiO 2 nanoparticles via utrasound-assisted sol-gel method," J. Chem. Pharm. Res., vol. 8, no. 2, pp. 620–626, 2016, [Online]. Available: www.jocpr.com
[30] D. P. Hansora, N. G. Shimpi, and S. Mishra, "Graphite to Graphene via Graphene Oxide: An Overview on Synthesis, Properties, and Applications," Jom, vol. 67, no. 12, pp. 2855–2868, 2015, doi: 10.1007/s11837-015-1522-5.
[31] D. Zhang, Z. Wu, and X. Zong, "Metal-organic frameworks-derived zinc oxide nanopolyhedra/S, N: graphene quantum dots/polyaniline ternary nanohybrid for high-performance acetone sensing," Sensors Actuators, B Chem., vol. 288, no. January, pp. 232–242, 2019, doi: 10.1016/j.snb.2019.02.093.
[32] H. Mohammadi, M. Ghaedi, M. Fazeli, and M. M. Sabzehmeidani, "Removal of hexavalent chromium ions and Acid Red 18 by superparamagnetic CoFe2O4/polyaniline nanocomposites under external ultrasonic fields," Microporous Mesoporous Mater., vol. 324, no. February, p. 111275, 2021, doi: 10.1016/j.micromeso.2021.111275.
[33] H. B. Desai, L. J. Hathiya, H. H. Joshi, and A. R. Tanna, "Synthesis and characterization of photocatalytic MnFe2O4 nanoparticles," Mater. Today Proc., vol. 21, pp. 1905–1910, 2020, doi: 10.1016/j.matpr.2020.01.248.
[34] S. S. Al-Taweel, H. R. Saud, A. A. H. Kadhum, and M. S. Takriff, "The influence of titanium dioxide nanofiller ratio on morphology and surface properties of TiO 2 /chitosan nanocomposite," Results Phys., vol. 13, no. February, p. 102296, 2019, doi: 10.1016/j.rinp.2019.102296.
[35] M. Khairy, "Synthesis, characterization, magnetic and electrical properties of polyaniline/NiFe2O4 nanocomposite," Synth. Met., vol. 189, pp. 34–41, 2014, doi: 10.1016/j.synthmet.2013.12.022.
[36] F. Farivar et al., "Unlocking thermogravimetric analysis (TGA) in the fight against 'Fake graphene' materials," Carbon N. Y., vol. 179, pp. 505–513, 2021, doi: 10.1016/j.carbon.2021.04.064.
[37] R. Bhattacharyya and S. K. Ray, "Removal of congo red and methyl violet from water using nano clay filled composite hydrogels of poly acrylic acid and polyethylene glycol," Chem. Eng. J., vol. 260, pp. 269–283, 2015, doi: 10.1016/j.cej.2014.08.030.
[38] A. S. Waheeb, H. A. H. Alshamsi, M. K. Al-Hussainawy, and H. R. Saud, "Myristica fragrans shells as potential low cost bio-adsorbent for the efficient removal of rose bengal from aqueous solution: Characteristic and kinetic study," Indones. J. Chem., vol. 20, no. 5, pp. 1152–1162, 2020, doi: 10.22146/ijc.50330.
[39] H. R. Mutar and K. K. Jasim, "Adsorption study of disperse yellow dye on nanocellulose surface," Mater. Today Proc., no. xxxx, pp. 1–7, 2022, doi: 10.1016/j.matpr.2021.04.003.
[40] J. van der Stap and S. Klaasse, "Labwaarden : Acute nierinsuffi ciëntie," Nursing (Lond)., vol. 22, no. 6, pp. 36–38, 2016, doi: 10.1007/s41193-016-0111-5.
[41] Muhammad A, Shah AU, Bilal S, Rahman G. Basic Blue dye adsorption from water using Polyaniline/Magnetite (Fe3O4) composites: Kinetic and thermodynamic aspects. Materials. 2019 May 30;12(11):1764.
[42] M. R. Kulkarni, T. Revanth, A. Acharya, and P. Bhat, "Removal of Crystal Violet dye from aqueous solution using water hyacinth: Equilibrium, kinetics and thermodynamics study," Resour. Technol., vol. 3, no. 1, pp. 71–77, 2017, doi:

10.1016/j.reffit.2017.01.009.
[43] H. Yu, J. Pang, T. Ai, and L. Liu, "Biosorption of Cu2+, Co2+ and Ni2+ from aqueous solution by modified corn silk: Equilibrium, kinetics, and thermodynamic studies," J. Taiwan Inst. Chem. Eng., vol. 62, pp. 21–30, 2016, doi: 10.1016/j.jtice.2016.01.026.
[44] M. L. Dlamini, M. Bhaumik, K. Pillay, and A. Maity, "Polyaniline nanofibers, a nanostructured conducting polymer for the remediation of Methyl orange dye from aqueous solutions in fixed-bed column studies," Heliyon, vol. 7, no. 10, p. e08180, 2021, doi: 10.1016/j.heliyon.2021.e08180.
[45] A. Hsini et al., "Elaboration of novel polyaniline@Almond shell biocomposite for effective removal of hexavalent chromium ions and Orange G dye from aqueous solutions," Environ. Sci. Pollut. Res., vol. 27, no. 13, pp. 15245–15258, 2020, doi: 10.1007/s11356-020-08039-1.
[46] R. Ahmad and R. Kumar, "Conducting polyaniline/iron oxide composite: A novel adsorbent for the removal of amido black 10b," J. Chem. Eng. Data, vol. 55, no. 9, pp. 3489–3493, 2010, doi: 10.1021/je1001686.
[47] F. S. Taheri, A. Ghaemi, A. Maleki, and S. Shahhosseini, "High CO2 adsorption on amine-functionalized improved mesoporous silica nanotube as an eco-friendly nanocomposite," Energy and Fuels, vol. 33, no. 6, pp. 5384–5397, 2019, doi: 10.1021/acs.energyfuels.9b00703.
[48] R. Asadi, H. Abdollahi, M. Gharabaghi, and Z. Boroumand, "Effective removal of Zn (II) ions from aqueous solution by the magnetic MnFe2O4 and CoFe2O4 spinel ferrite nanoparticles with focuses on synthesis, characterization, adsorption, and desorption," Adv. Powder Technol., vol. 31, no. 4, pp. 1480–1489, 2020, doi: 10.1016/j.apt.2020.01.028.